Identification and thermal healing of focused ion beam-induced defects in GaN using off-axis electron holography

K. Ji[1], M. Schnedler[1]*, Q. Lan[1], F. Zheng[1], Y. Wang[1], Y. Lu[1], H. Eisele[2], J.-F. Carlin[3], R. Butté[3], N. Grandjean[3], R. E. Dunin-Borkowski[1], and Ph. Ebert[1]

[1] *Ernst Ruska Centrum (ER-C-1) and Peter Grünberg Institut (PGI-5), Forschungszentrum Jülich GmbH, 52425 Jülich, Germany*

[2] *Institut für Physik, Otto-von-Guericke Universität Magdeburg, 39106 Magdeburg, Germany*

[3] *Institute of Physics, Ecole Polytechnique Fédérale de Lausanne, 1015 Lausanne, Switzerland*

Thermal healing of focused ion beam-implanted defects in GaN is investigated by off-axis electron holography in TEM. The data reveal that healing starts at temperatures as low as about 250 °C. The healing processes result in an irreversible transition from defect-induced Fermi level pinning near the valence band toward a midgap pinning induced by the crystalline-amorphous transition interface. Based on the measured pinning levels and the defect charge states, we identify the dominant defect type to be substitutional carbon on nitrogen sites.

During growth and processing of group III-nitride semiconductor devices a variety of point defects and impurities are incorporated intentionally as well as non-intentionally. Mostly, these defects and impurities compensate free carriers. This can be, on the one hand, desired, such as carbon can be used to create insulating layers in high electron mobility transistors (HEMTs).[1, 2, 3, 4] On the other hand, the devices' performance can be deteriorated by defect-induced recombination centers that reduce the quantum efficiency and shift the emission wavelength.[5, 6] Since the creation and incorporation of defects and impurities during processing cannot be avoided completely, it is critical to understand their dynamics and thermal healing behavior.

Therefore, we investigate point defects in group III-nitride semiconductors induced by focused ion beam (FIB). FIB is, on the one hand, widely used for the fabrication of nanoscale structures, with a particular focus on TEM sample preparation,[7] and, on the other hand, can be especially interesting for device fabrication due to its ability for local maskless implantation as well as the manipulation of nanoscale electrical connections.[8] In either application, FIB-induced defects can be anticipated to have a critical impact on

---

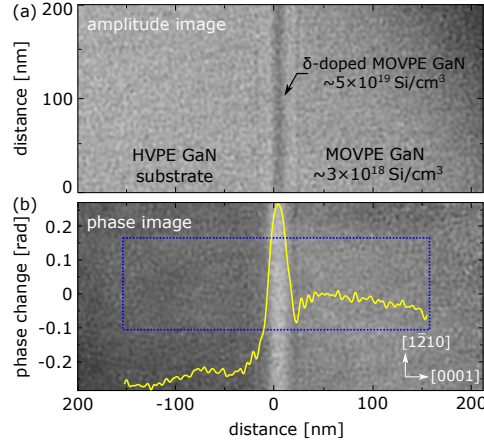*E-mail: m.schnedler@fz-juelich.de

Fig. 1. (a) Amplitude and (b) electron phase maps of lamella A1 recorded at 500 °C, reconstructed from 25 single holograms obtained by off-axis electron holography. The vertical contrast line at the substrate (left)-MOVPE-grown GaN (right) interface at 0 nm stems from a δ-doped like layer. The overlaid phase profile is extracted from a region free from dynamic diffraction contrast (marked by a blue dotted rectangle in (b)).

the electronic properties of the materials. We use off-axis electron holography in TEM to unravel the Fermi level pinning and a (0/-) charge transfer level of FIB-induced defects at surfaces of GaN lamellas. On this basis we conclude that the dominant electrically active pinning defect is in line with FIB-implanted substitutional carbon on nitrogen sites. In-situ annealing experiments reveal that the carbon impurities become mobile at temperatures as low as about 250 °C, lifting the Fermi level pinning.

For our experiments we used two different homostructures, labelled A and B, each consisting of a metal organic vapor phase epitaxy (MOVPE) grown GaN layer on a c-plane free-standing GaN pseudosubstrate [Fig. 1]. Epitaxial layer A (B) exhibits a Si doping of $5 \times 10^{19}\,\mathrm{cm}^{-3}$ ($2 \times 10^{19}\,\mathrm{cm}^{-3}$) in the first 20 nm (10 nm) [δ-doped like layer], followed by $3 \times 10^{18}\,\mathrm{cm}^{-3}$ in the remaining 700 nm (560 nm) thick layer, respectively, as determined by secondary ion mass spectrometry.[9] No dislocations or stacking faults were detected in the MOVPE-grown layers and scanning tunneling spectroscopy is in agreement with thermally activated Si dopants without compensating defects.[10, 11] From each GaN structure (A, B) two electron transparent lamellas (labelled A1, A2, B1, B2, respectively) were cut and milled using a FEI Helios Nanolab 400s dual-beam FIB system: A 2 µm thick carbon protection layer was deposited prior to the cutting and served as carbon source for implantation. The fine milling was performed with stepwise decreasing acceleration voltages of 30, 15, and 5 kV and grazing incident angles of 2,
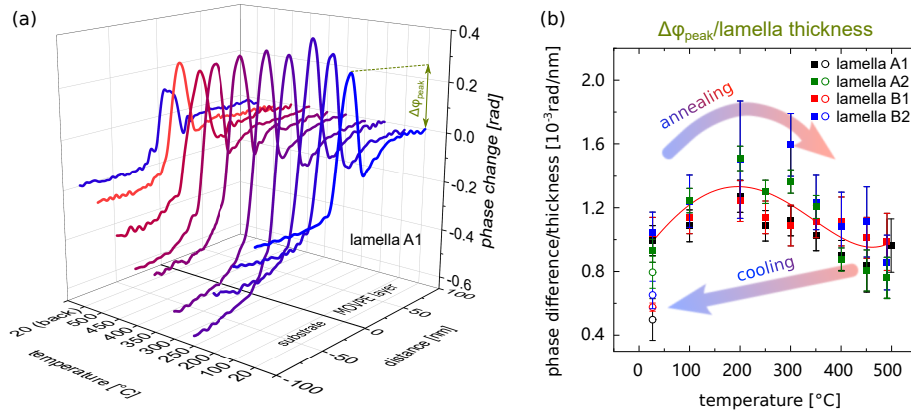
Fig. 2. (a) Electron phase profiles extracted in [0001] growth direction at different annealing temperatures. The delta-doped layer is at spatial position $0\,\mathrm{nm}$, where a phase peak appears. Distances larger (smaller) than zero correspond to the MOVPE-grown GaN layer (pseudosubstrate). (b) Reproducibility of the temperature dependent evolution of the phase peak height [$\Delta\varphi_{\mathrm{peak}}$ marked in (a)] normalized using the lamellas' crystalline thickness. Below (above) $\sim 250\,^\circ\mathrm{C}$, the phase difference increases (decreases).

1.2, and 5° of the Ga^+ ion beam, respectively, under simultaneous reduction of the current. After final preparation, lamella A1 was placed onto a heating chip used with a DENSsolutions double tilt heating holder, whereas the other lamellas were mounted on a Omniprobe half-grid to be used with a Gatan heating double tilt holder.

The crystalline thicknesses of the lamellas were determined using convergent beam electron diffraction (CBED), while the amorphous shell thicknesses were calculated by subtracting the thickness measured by CBED from that obtained in SEM. The results are given in the Supplementary Material. For example, lamella A1 displayed crystalline thicknesses of $(278 \pm 2)\,\mathrm{nm}$, accompanied by an amorphous outer shell measuring approximately $(9\pm5.1)\,\mathrm{nm}$ in thickness, consistent with previous findings.[9, 12]

Amplitude and electron optical phase maps, such as the ones shown in Fig. 1, were obtained from holograms acquired in an image-aberration-corrected FEI-Titan G2 60-300 HOLO microscope operated at 300 kV and equipped with an electron biprism,[13] using a reconstruction procedure described in Ref. [14]. The spatial resolution of the phase maps is 3.6 nm. In order to minimize diffraction contrast, the lamellas were tilted off the zone axis in edge-on orientation (see Supplementary Material). Phase change profiles were extracted only in regions without diffraction.

From the acquired phase maps we extracted profiles along the [0001] growth direction by integration along the perpendicular [$1\bar{2}10$] direction. For all phase profiles

we applied a linear background subtraction, using as reference the MOVPE layer. An examples is overlaid on the phase map in Fig. 1b (yellow line and left axis). In the following we focus on the spatial differences, i.e. changes of the electron phase between the different layers as a function of annealing. The temperature is increased in steps of typically 50°C each 30 min.

Figure 2(a) illustrates an overview of the temperature dependent changes of the phase profiles of lamella A1. The most prominent feature is the pronounced phase peak at the position of the δ-doped like layer (at spatial position 0 nm). The δ-doping enhances the electrostatic screening of the defect-induced electrostatic potential at the TEM lamellas' surfaces, thereby amplifying the phase contrast relative to the adjacent layers.[9] In our case no traces of polarization changes or strain are present and thus only doping governs the phase changes.[9, 15, 16] Here, we focus on the temperature evolution of the phase peak. The intensity of the phase peak relative to the remaining MOVPE-grown GaN [$\Delta\varphi_{\mathrm{peak}}$, Fig.2(a)] is found to increase first from 0.30 rad at RT to 0.38 rad at an annealing temperature of 250 °C. At higher temperatures, the intensity decreases again down to 0.25-0.28 rad. After cooling down back to RT, an obviously irreversible decrease of the intensity of the phase peak down to 0.14 rad occurred. The reproducibility of this behaviour has been experimentally confirmed across all four lamellas in Fig.2(b).

Note, the temperature evolution of the phase within the GaN pseudosubstrate in Fig. 2(a) varies significantly for different substrate locations, due to the presence of v-shaped defects and threading dislocations.[17] Therefore, we focus on the defect-free MOVPE-grown layer and the adjacent δ-doped layer, only.

Next we turn to a quantitative analysis of the temperature-dependent phase changes with the help of self-consistent simulations that are based on a two-step process:[9] First, the interaction of the built-in electrostatic potential as well as the potential at the lamella surfaces with the free and fixed carriers is determined by using a self-consistent finite-difference based Poisson solver, as described in Refs.[18, 19]. Note, the surface potential arises from FIB-induced defects pinning the Fermi energy. In a second step, the electron phase is calculated within the framework of the phase object approximation by integrating the obtained three dimensional electrostatic potential along the electron beam direction, followed by running average broadening of 4 nm in line with the measurement resolution.

The simulations' central physical parameters changing with temperature are the free

carrier concentration and the defect-induced charge transfer level E_{pin}, responsible for a surface Fermi level pinning relative to the valence band edge E_{V} (called "pinning level" in the following). All other parameters (e.g., lamella thickness and materials parameters, see Ref.[18]) are assumed to be temperature independent. The free carrier concentration is calculated self consistently using as input the concentrations of Si dopants and their thermal ionization. The charge transfer level is the only fitting parameter used in the following.

First we apply the simulations to the low temperature regime ($< 250°C$), where the intensity of the δ-doping induced phase peak increases with temperature. Figures 3(a,b) compare the measured temperature dependent phase profiles (colored symbols) with simulated ones (solid lines), illustrated exemplarily for lamella A1. The best agreement is found for almost unchanged pinning levels close to E_{V}. Thus, the increase in the phase peak height is solely due to the thermal increase of the free carrier concentration, i.e. by thermal activation of the Si dopants. This effect is taken into account for all further simulations and all temperatures.
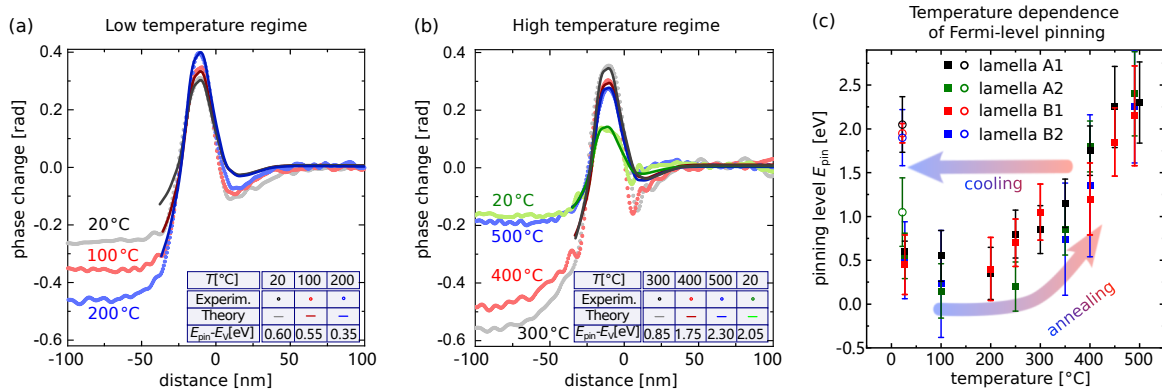

Fig. 3. (a, b) Comparison of experimental (symbols) and simulated (lines) electron phase profiles for lamella A1 in (a) the low temperature ($\leq 250\,°C$) and (b) the high temperature regime ($\geq 250\,°C$). The data after cooling back to room temperature is added in (b). (c) Temperature dependence of the pinning level E_{pin}, obtained by fitting simulated phase profiles to measured ones. The data points acquired after annealing and cooling to room temperature (open symbols) are shifted by -5 °C for clarity.

Second, in the high temperature regime [Fig. 3(b)], i.e. for 250 to 500 °C, the best agreement is obtained for pinning levels E_{pin} shifting toward the conduction band edge with temperature, reaching an energy position of $E_{\mathrm{V}} + 2.3$ eV, i.e. somewhat above midgap position.

Third, after cooling down back to room temperature, the pinning level remains above midgap.

Figure 3(c) illustrates the temperature dependence of the pinning levels E_{pin}. The data of both included lamellas agree quantitatively and reveal an overall increase of E_{pin} from $\sim 0.6\,\mathrm{eV}$ in the as prepared state to $\sim 2.3\,\mathrm{eV}$ at $500\,^{\circ}\mathrm{C}$. The pinning level remains at the high value of $\sim 2\,\mathrm{eV}$ even after cooling down to RT and after a second annealing cycle. Table I summarizes the pinning levels before and after annealing for all lamellas, corroborating the reproducibility of our findings.

lamella	E_{pin} at RT before annealing [eV]	E_{pin} at RT after annealing [eV]
A1	0.60±0.12	2.05±0.32
A2	0.55±0.26	1.05±0.39
B1	0.45±0.34	1.95±0.11
B2	0.50±0.44	1.90±0.32
weighted average	0.57±0.05	1.90±0.22

Table I.   Room-temperature Fermi energy pinning levels relative to E_{V} at the surfaces of as-prepared and 500°C-annealed TEM lamellas.

In order to understand the physical origin of the evolution of the Fermi level pinning, we recall the processes during FIB preparation: Ga^{+} ions are used to sputter the material to extract a thin lamella. It is well known that this results in an amorphous outer shell [Fig. 4(a)]. The amorphous outer shell can be anticipated to provide a midgap Fermi level pinning at the amorphous-crystalline transition region due to the multitudes of bonding structures and atom species [20] leading to a wide distribution of density of states in the band gap, with the neutrality level in its center.[21] However, the FIB-induced damages do not abruptly stop at the amorphous-crystalline interface. It can rather be anticipated that a defect-rich crystalline inner shell is formed, with a decaying concentration of point defects towards the lamellas' crystalline pristine core. These defects will pin the Fermi level at their respective charge transfer levels in the crystalline inner shell region.[9] Note, the pinning levels of the outer and inner shell are not necessarily identical. The critical pinning level that determines the phase contrast is that of the inner defect-rich crystalline shell, as its potential is screened by the free charge carrier in the enclosed defect-free pristine crystalline core.

It should be noted that the amorphous outer shell, the defect-rich electrically inactive inner shell, and the screening region in the defect-free pristine core region below are either fully or partially considered previously[22, 23, 24, 25] as "dead layer".
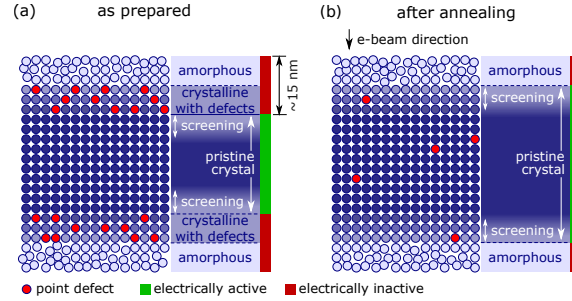

Fig. 4. Cross-sectional schematic view of the different FIB-induced shell structure of a TEM lamella in the as-prepared (a) and annealed state (b). FIB preparation results in an amorphous outer shell (light blue circles) covering a crystalline core (dark blue circles). In the as-prepared state (a) directly below the amorphous shell (mid blue circles) is a further inner crystalline shell that contains a large concentration of FIB-induced point defects (red circles), leading to a Fermi level pinning near the valence band and thus a surface potential. This defect-rich crystalline inner shell is electrically inactive (red zone). The surface potential is screened by the free charge carriers in the following enclosed defect-free pristine crystalline core (green zone). The total thickness of the electrically dead layer (amorphous outer plus defect-rich inner shell) can be estimated from calculations of the stopping and range of ions/transport of ions in matter (see Supplementary Material), which confirm that surface carbon is implanted with a penetration depth of up to 15 nm. (b) After annealing the defects in the defect-rich crystalline shell healed, restoring the pristine crystal and only the amorphous outer shell induces a surface potential with mid-gap Fermi level pinning.

It can be expected that the amorphous outer shell does not recrystallize during annealing, since the temperatures are well below the onset of recrystallization of typically 40% of the melting temperature.[26] We did not observe either the formation of Ga agglomerates. Hence, the temperature dependence of electron optical phase reflects changes in the crystalline inner shell: Upon annealing the defects in the electrically inactive crystalline inner shell can be anticipated to become mobile, healing/restoring the pristine properties of the material,[27] as shown schematically in Fig. 4(b). In this framework, the temperature dependence of the pinning level E_{pin} is directly related to concentration changes by thermally activated mobility of the FIB-induced point defects in the electrically inactive defect-rich crystalline inner shell. In particular, the change observed above a temperature of about 250 °C suggests an onset of point defect motion.

This raises the question of the dominant type of point defect. The defect type can

be identified using (i) the measured pinning level about 0.6 eV above E_V and (ii) the derived type of charge transfer level: For n-type GaN a surface pinning can only be achieved by a defect that exhibits a charge transfer towards a negative charge state in the band gap.[28] The simplest one is the (0/-) charge transfer level. Based on these two criteria we assess different types of point defects:

First, intrinsic point defects, i.e. Ga vacancy (V_{Ga}), N vacancy (V_N), N interstitial (N_i), Ga interstitial (Ga_i), N antisite (N_{Ga}), and Ga antisite (Ga_N), have only charge transfer levels involving positive charge states in the lower half of the band gap.[29, 30, 31, 32] Notably, the V_N suggested previously,[9] has (+/3+) charge transfer level at 0.7 eV, which however cannot pin the Fermi energy for n-type GaN as outlined above.[31, 32] Hence, intrinsic point defects cannot be at the origin of the observed pinning level near E_V in n-type GaN.

Second, we address impurities. Oxygen and hydrogen possibly present due to prior air (and water) exposure could be implanted during FIB preparation. However, oxygen in GaN is an n-type dopant and thus cannot induce the observed pinning deep inside the band gap,[33] while hydrogen has no charge transfer level in the band gap.[34] Another source of impurity could stem from protective carbon layers and carbon contamination films deposited onto the samples in the course of our FIB preparation. The implantation of C into the crystalline inner shell of the lamellas is corroborated by calculations of the stopping and range of ions/transport of ions in matter (SRIM/TRIM)[35] that confirm C penetration of up to 15 nm (see Supplementary Material). Due to the fact that C on nitrogen sites has the lowest formation energy for Ga-rich conditions[36] present in a Ga FIB, we anticipate that a high fraction of C occupies nitrogen sites (C_N). C_N is predicted to have the (0/-) charge transfer level ~ 0.8 eV above E_V,[6, 36, 37] in good agreement with the observed pinning level of 0.57 eV above E_V. Hence, in view of all other defect levels not exhibiting suitable charge transfer levels and the abundant presence of carbon, we conclude that the Fermi level pinning in the defect-rich crystalline inner shell is due to carbon implantation. Note, even W or Pt protective layers contain high concentrations of carbon, due to the used precursors.

Mobility induced by annealing reduces the C_N concentration, eventually falling below the doping concentration. Thereby the C_N-induced near surface Fermi level pinning is lifted. As a consequence, the pinning level E_{pin} shifts from its C_N-induced value close to E_V towards a midgap position arising from the crystalline-amorphous transition region.

In conclusion, freshly FIB-prepared GaN lamellas exhibit a Fermi level pinning of 0.57 eV above E_V, attributed to the implantation of C_N during FIB. The pinning level gradually increases from 0.57 to about 2 eV above E_V upon annealing between 250 and 500°C and remains high after cooling down to room temperature. This indicates an irreversible thermal healing, gradually reducing the implanted C_N concentration and hence lifting the C_N-induced Fermi level pinning. The dominating higher midgap pinning level is attributed to amorphous shell-crystalline core interface states. The results demonstrate that temperatures as low as about 250°C are sufficient to initiate defect healing.

Acknowledgement

References

[1] M. Huber et al. *Appl. Phys. Lett.* 107 (2015), 032106. DOI: `10.1063/1.4927405`.

[2] B. Rackauskas et al. *IEEE Trans Electron Devices* 65 (2018), 1838–1842. DOI: `10.1109/TED.2018.2813542`.

[3] G. Verzellesi et al. *IEEE Electron Device Lett.* 35 (2014), 443–445. DOI: `10.1109/LED.2014.2304680`.

[4] F. Kaess et al. *J. Appl. Phys.* 120 (2016), 105701. DOI: `10.1063/1.4962017`.

[5] D. O. Demchenko et al. *Phys. Rev. Lett.* 110 (2013), 087404. DOI: `10.1103/PhysRevLett.110.087404`.

[6] J. Lyons et al. *Appl. Phys. Lett.* 97 (2010), 152108. DOI: `10.1063/1.3492841`.

[7] L. A. Giannuzzi et al. *Microsc. Res. Tech.* 41 (1998), 285–290. DOI: `10.1002/(SICI)1097-0029(19980515)`.

[8] J. Koch et al. "Creation of nanoelectronic devices by focussed ion beam implantation". In: *Proceedings of IECON'99, 25th Annual Conference of the IEEE Industrial Electronics Society.* Vol. 1. 1999, 35–39. DOI: `10.1109/IECON.1999.822165`.

[9] Y. Wang et al. *Phys. Rev. B* 102 (2020), 245304. DOI: `10.1103/PhysRevB.102.245304`.

[10] M. Schnedler et al. *Phys. Rev. B* 91 (2015), 205309. DOI: `10.1103/PhysRevB.91.205309`.

[11]   L. Freter et al. *J. Appl. Phys.* 128 (2020), 185701. DOI: 10.1063/5.0020652. eprint: https://doi.org/10.1063/5.0020652.

[12]   D. A. Cullen et al. *J. Appl. Phys.* 104 (2008), 094304. DOI: 10.1063/1.3006626. eprint: https://doi.org/10.1063/1.3006626.

[13]   Ernst Ruska-Centre for Microscopy and Spectroscopy with Electrons (ER-C). *Journal of large-scale research facilities* 2 (2016), A44. DOI: 10.17815/jlsrf-2-70.

[14]   R. E. Dunin-Borkowski et al. "Springer Handbook of Microscopy". In: ed. by P. W. Hawkes et al. Springer Handbook. Springer, Cham, 2019. Chap. 16. Electron Holography, 767–818. ISBN: 978-3-030-00068-4. DOI: 10.1007/978-3-030-00069-1.

[15]   V. Boureau et al. *J. Appl. Phys.* 128 (2020), 155704. DOI: 10.1063/5.0020717.

[16]   D. Cooper et al. *Nanotechnology* 31 (2020), 475705. DOI: 10.1088/1361-6528/abad5f.

[17]   P. H. Weidlich et al. *Appl. Phys. Lett.* 103 (2013), 062101. DOI: http://dx.doi.org/10.1063/1.4816969.

[18]   M. Schnedler et al. *Phys. Rev. B* 91 (2015), 235305. DOI: 10.1103/PhysRevB.91.235305.

[19]   M. Schnedler et al. *Phys. Rev. B* 93 (2016), 195444. DOI: 10.1103/PhysRevB.93.195444.

[20]   B. Cai et al. *Phys. Rev. B* 84 (2011), 075216. DOI: 10.1103/PhysRevB.84.075216.

[21]   W. Walukiewicz. *Physica B* 302-303 (2001), 123.

[22]   L. Houben et al. *Phys. Rev. B* 70 (2004), 165313. DOI: 10.1103/PhysRevB.70.165313.

[23]   W. D. Rau et al. *Phys. Rev. Lett.* 82 (1999), 2614–2617. DOI: 10.1103/PhysRevLett.82.2614.

[24]   A. C. Twitchett et al. *Phys. Rev. Lett.* 88 (2002), 238302. DOI: 10.1103/PhysRevLett.88.238302.

[25]   K. Yamamoto et al. *Microscopy* 69 (2019), 1–10. DOI: 10.1093/jmicro/dfz037.

[26]   H. Oettel et al. *Metallografie: Mit einer Einführung in die Keramografie.* Weinheim: Wiley-VCH, 2011. ISBN: 978-3-527-32257-2.

[27]   D. Cooper et al. *Appl. Phys. Lett.* 88 (2006), 063510. DOI: 10.1063/1.2172068.

[28]   W. Mönch. *Semiconductor Surfaces and Interfaces.* 3rd Edition. Berlin: Springer, 2001.

[29]   D. C. Look et al. *Mater. Sci. Eng.* 66 (1999), 30–32. DOI: `10.1016/S0921-5107(99)00115-4`.

[30]   T. Mattila et al. *Phys. Rev. B* 55 (1997), 9571. DOI: `10.1103/PhysRevB.55.9571`.

[31]   S. Limpijumnong et al. *Phys. Rev. B* 69 (2004), 035207. DOI: `10.1103/PhysRevB.69.035207`.

[32]   J. L. Lyons et al. *npj Comput. Mater.* 3 (2017), 12. DOI: `10.1038/s41524-017-0014-2`.

[33]   T. Mattila et al. *Phys. Rev. B* 54 (1996), 16676. DOI: `10.1103/PhysRevB.54.16676`.

[34]   C. G. Van de Walle. *Phys. Rev. B* 56 (1997), R10020. DOI: `10.1103/PhysRevB.56.R10020`.

[35]   J. F. Ziegler et al. *Nucl. Instrum. Methods Phys. Res. B* 268 (2010), 1818–1823. ISSN: 0168-583X. DOI: `https://doi.org/10.1016/j.nimb.2010.02.091`.

[36]   J. L. Lyons et al. *Phys. Rev. B* 89 (2014), 035204. DOI: `10.1103/PhysRevB.89.035204`.

[37]   M. Matsubara et al. *J. Appl. Phys.* 121 (2017), 195701. DOI: `doi.org/10.1063/1.4983452`.